

Flux Estimates and Detection Prospects for Lunar Geoneutrinos

Hang Hu,¹ Yaping Cheng,^{2,*} and Wan-Lei Guo^{3,†}

¹*Guangdong Ocean University, Zhanjiang, 524088, China*

²*Beijing Institute of Spacecraft Environment Engineering, Beijing, 100094, China*

³*Institute of High Energy Physics, Chinese Academy of Sciences, Beijing 100049, China*

(Dated: March 3, 2026)

The distribution of heat-producing elements (U, Th, K) within the Moon is critical for understanding its thermal evolution and formation history. Based on a refined lunar interior model, we calculate the geoneutrino fluxes at two representative detector locations that bracket the expected signal intensity. The maximum flux is found to be slightly lower than the corresponding predicted fluxes for the KamLAND site on Earth, while the minimum flux is approximately a factor of 8.63 lower than this maximum value. The angular distributions of geoneutrinos arriving at the two locations were further computed. Finally, we evaluate the detection prospects for lunar geoneutrinos using three reaction channels: inverse beta decay reaction, elastic scattering on electrons, and a novel radiochemical approach based on $\bar{\nu}_e + {}^3\text{He} \rightarrow e^+ + {}^3\text{H}$. For each reaction, we calculate the expected event rates and briefly discuss the potential for measuring the total geoneutrino flux, as well as the relative contributions from U, Th, and K.

I. INTRODUCTION

The Moon exhibits a striking global dichotomy between its nearside and farside hemispheres, a feature that is fundamental to understanding planetary differentiation [1]. The lunar surface is geochemically divided into three major provinces [2]. The nearside is dominated by the Procellarum KREEP Terrane (PKT), a region characterized by extensive mare volcanism, high heat flow, and significantly enriched concentrations of heat-producing elements (HPEs) such as Uranium (U), Thorium (Th), and Potassium (K) [3–5]. In contrast, the farside Feldspathic Highlands Terrane (FHT) is anorthositic, structurally thicker, and depleted in radioactive elements, representing the primordial lunar crust [6–8]. A third distinct province, the South Pole-Aitken (SPA) basin, represents a massive impact structure that exposes deep crustal or upper mantle materials with unique compositional properties [9, 10].

This asymmetry is fundamentally linked to the crystallization of the lunar magma ocean and the subsequent concentration of incompatible elements—Potassium, Rare Earth Elements, and Phosphorus (KREEP)—into the final residual melt [11]. The uneven distribution of this radiogenic KREEP layer is hypothesized to have driven the prolonged volcanic activity observed in the PKT [1]. Understanding the precise 3D distribution of these elements is essential for constraining models of the Moon’s formation and thermal history. While recent missions like Chang’e-5 have returned young basalts from the nearside [12], the recently completed Chang’e-6 mission has returned the first samples from the lunar farside, revealing distinct volcanic episodes at 2.8 Ga and 4.2 Ga that challenge previous thermal models [13, 14].

Despite these advances, a global, deep-interior perspective remains necessary to resolve ambiguities regarding the bulk abundance of HPEs. Just as on Earth, the detection of lunar geoneutrinos offers a unique, direct probe to map these reservoirs and advance our understanding of lunar evolution [15–17].

The radioactive decay of naturally occurring isotopes (${}^{238}\text{U}$, ${}^{232}\text{Th}$, and ${}^{40}\text{K}$) is a primary heat source driving planetary thermal evolution [15, 16]. These decays emit geoneutrinos (electron antineutrinos, $\bar{\nu}_e$), which traverse planetary bodies unimpeded, carrying information about the abundance and distribution of their parent isotopes. On Earth, the KamLAND experiment achieved the first detection of geoneutrinos in 2005, reporting a 90% confidence interval of 4.5 to 54.2 events, which was consistent with geophysical predictions of 19 events [18]. Subsequent advancements were marked by the Borexino and KamLAND experiments, which observed geoneutrinos with high statistical significance. Borexino detected 53 events [19] and KamLAND 183 [20], with both achieving a relative precision on the measured rate between 15% and 18%. In the near future, JUNO will measure the total geoneutrino flux with a world-leading precision of about 8% over ten years [21]. Detecting mantle neutrinos at 3σ within six years, for the highest-concentration models, requires constraining the lithospheric flux to better than 15% [21].

The Moon’s internal heat sources remain poorly constrained, with Apollo 15 and 17 heat flow measurements indicating surface fluxes of approximately 21–28 mW/m² [22], but the relative contributions from radiogenic decay, primordial accretion heat, and ongoing tidal interactions with Earth are actively debated among scientists. This uncertainty stems from limited direct sampling, variable crustal enrichment in heat-producing elements post-giant impact formation, and questions about the Moon’s core and mantle dynamics [23]. Recent research highlights the role of tidal heating, revealing an ultralow-viscosity zone at the core-mantle bound-

* applelovei@qq.com

† guowl@ihep.ac.cn

ary where Earth’s gravitational pull generates significant heat, suggesting the Moon’s deep interior remains warm and partially molten rather than fully solidified as previously assumed [24]. Extending this geoneutrino detection technique to the Moon would allow for the measurement of the total lunar geoneutrino flux, the refractory Th/U ratio, and the volatile K abundance. Such measurements would serve to experimentally verify these theoretical models. Furthermore, disentangling crustal and mantle contributions could resolve debates regarding the enrichment of the lunar mantle beneath the PKT, the overall bulk composition inherited from the giant impact hypothesis, and the thermal state of the core [2, 25].

This study aims to estimate the geoneutrino fluxes on the Moon and evaluate detection prospects using diverse reaction channels. We utilize updated lunar interior models constrained by gravity, topography, and magnetic data to calculate fluxes at key locations. A major innovation of this work is the proposal to utilize in-situ lunar ^3He resources as a target for detecting low-energy geoneutrinos, including the ^{40}K component, via radiochemical methods. We structure the paper as follows. Section II details the U, Th, and K distribution model. In Section III, we calculate the geoneutrino fluxes and angular distributions. Section IV discusses detection prospects via three distinct reaction channels. Finally, a summary is given in Section V.

II. DISTRIBUTIONS OF TH, U AND K

To calculate geoneutrino fluxes, we adopt the “Model 5” for the HPEs distribution inside the Moon, the preferred model among the five different models developed in Ref. [4]. This model was constructed by integrating multiple constraints: crustal thickness from GRAIL gravity data, surface Th abundances from Lunar Prospector gamma-ray spectrometer measurements, Apollo sample analyses, recent crustal magnetization inversions, and mass balance considerations assuming Earth-like bulk refractory element abundances inside the Moon. Specifically, the model assumes lower Th in the deep highland crust compared to surface values to ensure sufficient radiogenic heat remains in the mantle for prolonged volcanic activity, including on the farside. The PKT crust is divided into an inner region with higher Th enrichment (corresponding to the low-magnetization zone identified from magnetic field data) and an outer region, allowing the inner PKT to experience delayed cooling below the Curie temperature of iron until after the lunar dynamo’s high-field epoch declined around 3.56 Ga. When tested with 3D thermochemical convection simulations, Model 5 best reproduces key observables among five candidate distributions, including the asymmetric and long-duration volcanism (lasting until 1-2 Ga on the near-side and 3 Ga on the farside), the paleomagnetic record of crustal magnetization, the Apollo heat flow measurements, and a sustained core dynamo for 1 billion years

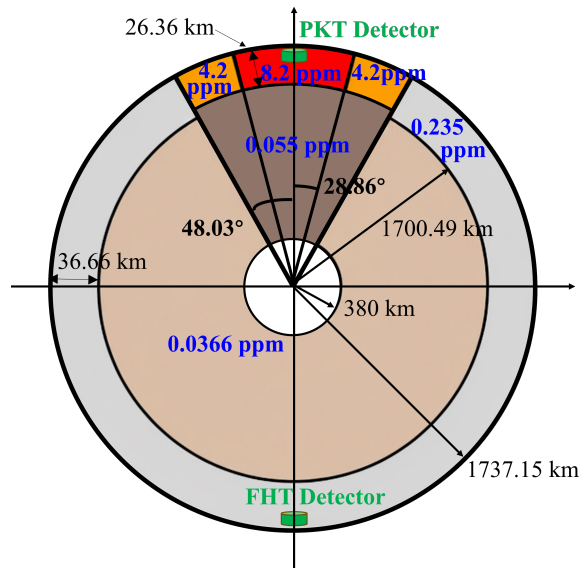


FIG. 1. Schematic cross-section of the lunar interior illustrating the Th distribution in Model 5. The PKT crust is divided into an inner region (8.2 ppm Th, angular extent 28.86° from the axis) and outer region (4.2 ppm Th, extending to 48.03°), with the underlying PKT mantle slightly enriched (0.055 ppm Th) compared to the highland mantle (0.0366 ppm Th). The FHT crust has 0.235 ppm Th. A small core (380 km radius) is shown, and hypothetical geoneutrino detectors are placed in the PKT and FHT regions. This axisymmetric geometry captures the hemispheric asymmetry while simplifying the irregular PKT shape for calculations.

followed by episodic activity [4].

As shown in Fig. 1, Model 5 defines the distribution of Th across five distinct geochemical reservoirs with the following concentrations [4]:

1. **FHT Crust:** 0.235 ppm Th. This value is lower than surface estimates (~ 1 ppm) to account for the predominantly anorthositic composition of the deep crust.
2. **PKT Outer Crust:** 4.2 ppm Th.
3. **PKT Inner Crust:** 8.2 ppm Th. This enrichment corresponds to the composition of mafic impact-melt breccias and accounts for the observed low magnetization.
4. **FHT Mantle:** 0.0366 ppm Th.
5. **PKT Mantle:** 0.0550 ppm Th. This enrichment relative to the highland mantle accounts for the source regions of mare basalts.

The U and K abundances can be derived from Th using fixed global ratios. We assume a chondritic refractory ratio of $\text{Th}/\text{U} \approx 3.7$ [26], which is consistent with both Earth and Moon compositions as these refractory elements did not fractionate significantly during the Moon’s formation via giant impact. For potassium, we adopt a

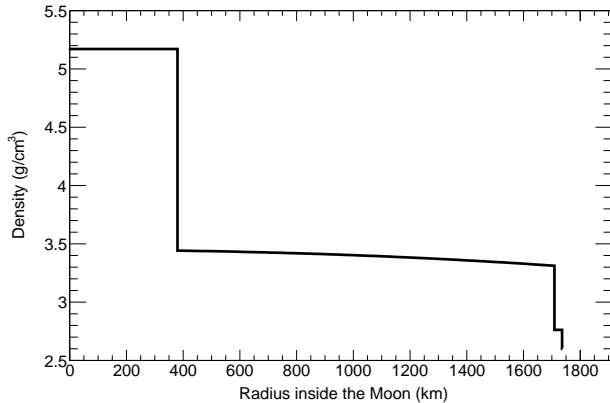


FIG. 2. Lunar density versus radius.

bulk Moon K/Th ratio of 460 [4], reflecting the Moon’s depletion in moderately volatile elements compared to Earth (where K/Th \approx 3000 [27]) due to high-temperature processing and volatile loss in the protolunar disk. In our calculations, the Moon is modeled as a sphere with a radius of 1737.15 km. The crustal thicknesses of the PKT and FHT are 26.36 km and 36.66 km [28], respectively. Base on the Lunar density profile [29] in Fig. 2, we integrate the total mass of ^{232}Th , ^{238}U , and ^{40}K in each of the five reservoirs to normalize the source strength for flux calculations, as listed in Table I.

Reservoir	^{232}Th	^{238}U	^{40}K
PKT Inner Crust	1.41×10^{15}	3.78×10^{14}	7.59×10^{13}
PKT Outer Crust	1.20×10^{15}	3.22×10^{14}	6.46×10^{13}
FHT Crust	7.69×10^{14}	2.06×10^{14}	4.14×10^{13}
PKT Mantle	6.35×10^{14}	1.70×10^{14}	3.42×10^{13}
FHT Mantle	2.09×10^{15}	5.61×10^{14}	1.12×10^{14}
Total	6.11×10^{15}	1.64×10^{15}	3.29×10^{14}

TABLE I. Masses of ^{232}Th , ^{238}U and ^{40}K per reservoir (kg).

Note that Model 5 simplifies the PKT geometry into concentric cones and uses highland values to approximate the SPA basin properties, ensuring computational efficiency. Despite these approximations, it effectively captures the essential hemispherical asymmetry needed for accurate flux estimation [4]. Additional simplifications include assuming uniform densities within the crust and mantle (ignoring minor lateral variations), a fixed core radius of 380 km without HPEs, and neglecting post-magma ocean processes like mantle overturn for initial condition setup.

III. LUNAR GEONEUTRINO FLUXES

The differential geoneutrino flux $\phi_i(E_{\bar{\nu}_e}, \vec{d})$ at a detector position \vec{d} can be calculated by integrating the contributions from all source volumes V within the Moon. The flux formula is given by [15, 16]:

$$\phi_i(E_{\bar{\nu}_e}, \vec{d}) = \int_V \frac{A_i(\vec{r}) C_i}{\tau_i m_i} f_i(E_{\bar{\nu}_e}) P_{ee} \frac{\rho(\vec{r})}{4\pi|\vec{r} - \vec{d}|^2} dV, \quad (1)$$

where $A_i(\vec{r})$ is the abundance of the i th HPEs at position \vec{r} , C_i , τ_i and m_i are the isotopic concentration, lifetime and mass of nucleus i . The lunar density $\rho(\vec{r})$ can be obtained from Fig. 2. $f_i(E_{\bar{\nu}_e})$ is the differential energy spectrum of the produced geoneutrino per decay chain [30]. For neutrino oscillations, we adopt an average electron antineutrino survival probability of $\langle P_{ee} \rangle \approx 0.5486$. This value is updated based on the latest precision measurements of mixing angles θ_{12} and θ_{13} from the Daya Bay and JUNO experiments [31, 32]. This formulation accounts for the production rate of antineutrinos from beta decays in radiogenic isotopes while propagating through the lunar interior with negligible absorption.

We calculate the geoneutrino fluxes for two potential detector locations to bracket the signal intensity: the center of the PKT (maximum flux due to local crustal enrichment) and the center of the FHT (minimum flux), as shown in Fig. 1. The detector overburden of 50 m is chosen based on the typical depth of lunar lava tubes [33], which offer a naturally shielded environment for potential lunar bases and neutrino detectors. A distinct advantage of a lunar-based neutrino experiment is the suppression of cosmic ray backgrounds. Due to the lack of a lunar atmosphere, a detector burial depth of only 50 m on the Moon provides a reduction in muon flux comparable to or better than the 1000 m overburden at the KamLAND site on the Earth [34].

In Fig. 3, we plot the differential geoneutrino spectra for the PKT and FHT detectors. It is found that the geoneutrino flux at the PKT detector is higher than that at the FHT detector by a factor of 8.63. The PKT detector experiences the highest flux because it is situated directly above the region with the greatest concentration of HPEs, leading to enhanced local antineutrino production from the enriched inner and outer PKT crust. Conversely, the FHT detector registers the lowest flux as it overlies the feldspathic highlands with significantly lower radiogenic element abundances, resulting in a dominant contribution from the more distant and dilute mantle sources. From Fig. 3, the integrated geoneutrino fluxes at the PKT and FHT detectors are determined to be $4.21 \times 10^6 \text{ cm}^{-2}\text{s}^{-1}$ and $4.88 \times 10^5 \text{ cm}^{-2}\text{s}^{-1}$, respectively. For the PKT detector, the contributions from the ^{238}U and ^{232}Th decay chains are calculated as $1.72 \times 10^6 \text{ cm}^{-2}\text{s}^{-1}$ and $1.38 \times 10^6 \text{ cm}^{-2}\text{s}^{-1}$. These values are slightly lower than the corresponding predicted fluxes of $2.34 \times 10^6 \text{ cm}^{-2}\text{s}^{-1}$ and $1.98 \times 10^6 \text{ cm}^{-2}\text{s}^{-1}$ for the KamLAND site on Earth [18].

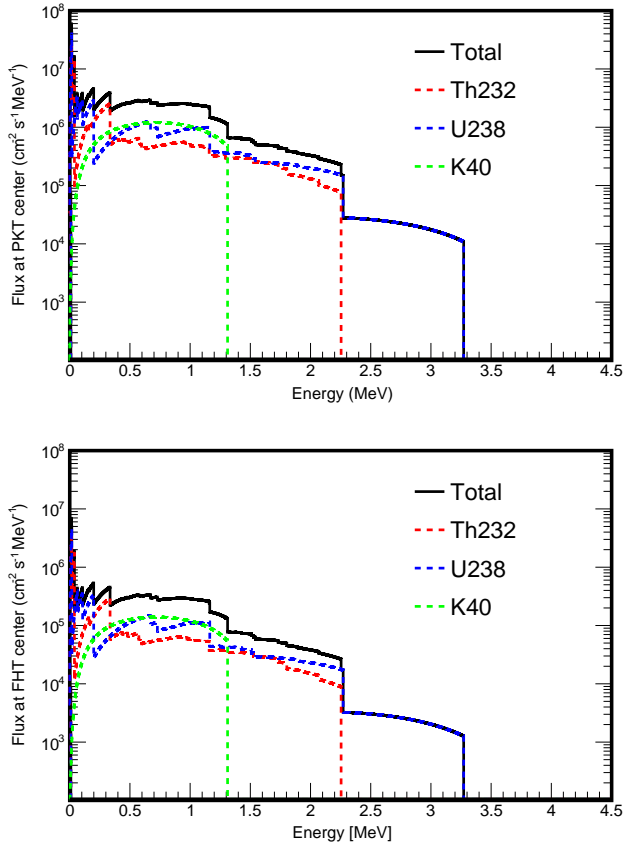


FIG. 3. Geoneutrino energy spectra for the PKT detector (top) and FHT detector (bottom), showing contributions from ^{232}Th , ^{238}U , and ^{40}K .

The cumulative geoneutrino fluxes as a function of the distance from the PKT and FHT detectors have been plotted in Fig. 4. For the PKT case, the PKT inner crust contributes almost all the geoneutrinos within 1000 km. This rapid accumulation stems from the physics of source proximity: the PKT inner crust, with its high emissivity and lateral extent ($\sim 28.86^\circ$ angular radius, corresponding to ~ 862 km surface arc length at lunar radius 1710.79 km), encompasses most high HPE sources within intermediate distances. For the FHT detector, within 100 km, the FHT crust contributes most to the total signal, reflecting the immediate subsurface layer’s role despite low HPEs. At a distance of 1000 km, the contributions from the FHT crust and FHT mantle become almost equal, as the cumulative integral incorporates extended crustal regions and the underlying mantle, whose larger homogeneous volume compensates for lower emissivity over mid-range distances. This parity highlights the transition from local crustal dominance to volumetric mantle influence in low HPE regions. These spatial patterns resonate with terrestrial geoneutrino observations [35, 36], where cumulative fluxes at continental sites (analogous to the lunar PKT) receive approximately 50% of their signal from within a 500 km radius due to the presence of

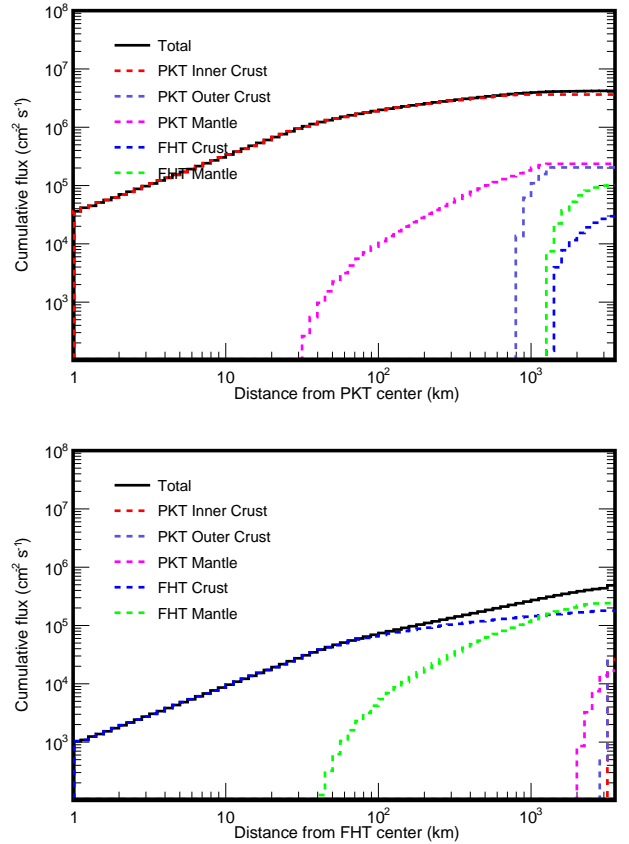


FIG. 4. Cumulative geoneutrino fluxes as functions of the distance from the PKT (top) and FHT (bottom) detectors, showing contributions from five distinct reservoirs.

thick, radioelement-enriched crust. In contrast, oceanic or thin-crust sites (analogous to the FHT) is less localized and features a non-negligible far-field mantle component. The Moon’s compact geometry amplifies the angular resolution of crustal heterogeneities like the PKT, yet simultaneously demands directional detection to partition the superimposed signals from layered interior reservoirs.

The capability to measure the direction of incident geoneutrinos would provide significant benefits. Directional sensitivity allows for the separation of the FHT crustal signal from the FHT mantle signal, as can be seen in Fig. 5. The FHT crust geoneutrinos peak at near-horizontal incident angles ($\cos\theta = 0$), while the FHT mantle geoneutrinos would be dominant over a range of angles below the horizontal ($\cos\theta < -0.4$). It is clear that directional detection capability would enable a tomography of the lunar interior. For the PKT detector, the PKT outer crust can give a significant contribution in the range of $-0.4 < \cos\theta < -0.3$. Directional detection of geoneutrinos from this direction can help constrain the boundaries of the enriched Inner PKT region, thus verifying heat source distribution models [4]. Furthermore, this directionality aids in subtracting residual backgrounds (e.g., solar and potential reactor neutrinos)

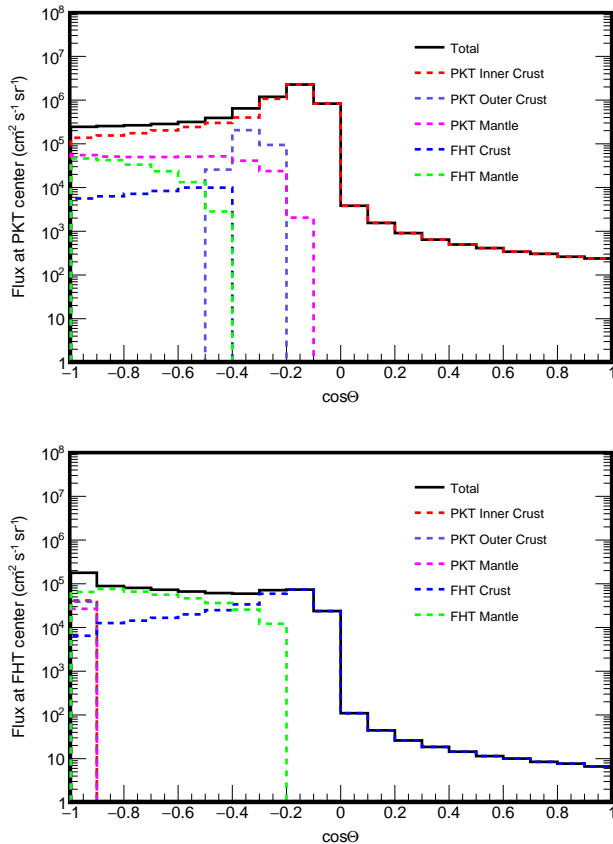


FIG. 5. Angular distributions of geoneutrinos at the PKT (top) and FHT (bottom) detectors from five reservoirs.

and could probe deeper structures, such as core contributions or asymmetries in HPEs distribution, as demonstrated in terrestrial studies with direction-sensitive detectors [37, 38].

IV. DETECTION PROSPECTS FOR LUNAR GEONEUTRINOS

In this section, we shall estimate the expected event rates and detection prospects for lunar geoneutrinos through three distinct interaction channels:

1. $\bar{\nu}_e + p \rightarrow e^+ + n$ (Inverse Beta Decay, IBD);
2. $\bar{\nu}_e + {}^3\text{He} \rightarrow e^+ + {}^3\text{H}$ (IBD reaction on ${}^3\text{He}$);
3. $\bar{\nu} + e^- \rightarrow \bar{\nu} + e^-$ (Elastic Scattering, ES).

Based on the distinct characteristics of these reactions and their corresponding detection techniques, we further evaluate the detector exposure (in kiloton-years) required to achieve specific physical goals on the Moon, such as measuring the total geoneutrino flux or determining the individual contributions from U, Th, and K.

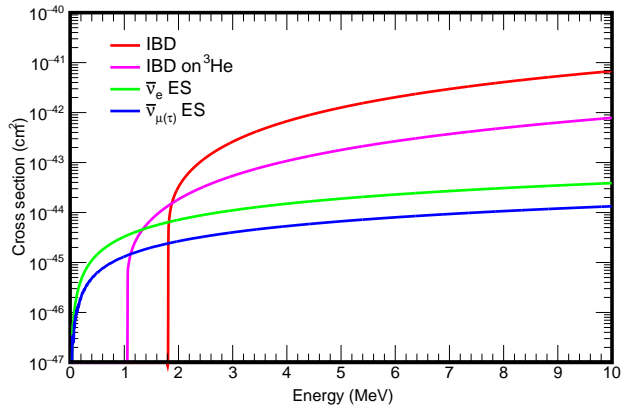


FIG. 6. Antineutrino cross sections for three interaction channels: IBD reaction with 1.806 MeV threshold, IBD reaction on ${}^3\text{He}$ with 1.041 MeV threshold and elastic scattering of $\bar{\nu}_e$ and $\bar{\nu}_{\mu(\tau)}$ on electrons with no energy threshold.

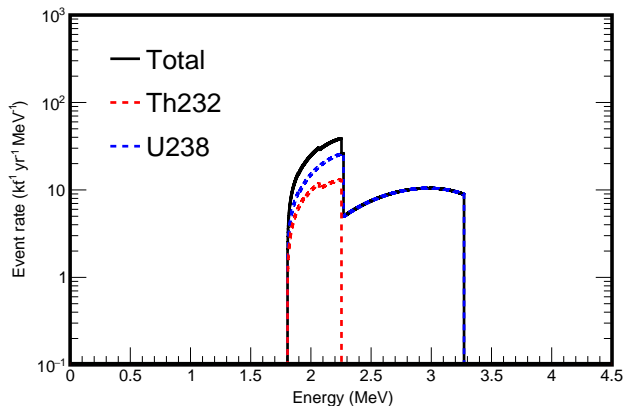


FIG. 7. IBD event rates from ${}^{238}\text{U}$ and ${}^{232}\text{Th}$ at the PKT site.

A. IBD reaction on free protons

The IBD reaction, $\bar{\nu}_e + p \rightarrow e^+ + n$, serves as the primary channel for geoneutrino detection on Earth due to its relatively large interaction cross section [39], as shown in Fig. 6, and the powerful background rejection offered by its distinct prompt-delayed coincidence signature in the liquid scintillator detectors [18–21]. However, a fundamental limitation of this channel is its energy threshold of 1.806 MeV. This threshold renders the reaction sensitive exclusively to geoneutrinos originating from the decay chains of ${}^{238}\text{U}$ and ${}^{232}\text{Th}$, while leaving the detector blind to the flux from ${}^{40}\text{K}$ decays, which possess a maximum energy of approximately 1.31 MeV.

Assuming a liquid scintillator detector composed of 88% ${}^{12}\text{C}$ and 12% ${}^1\text{H}$ [40], we calculate the expected IBD event rates for the PKT site, as shown in Fig. 7. The total rate is found to be $20.58 \text{ kt}^{-1} \text{ yr}^{-1}$, where ${}^{238}\text{U}$ and ${}^{232}\text{Th}$ respectively contribute 16.44 and $4.15 \text{ kt}^{-1} \text{ yr}^{-1}$. This

rate for a PKT detector on Moon is about 49% of that for the proposed Jinping Neutrino Experiment (JNE) on Earth [41]. Applying the JNE sensitivity analysis and assuming the same background level, we roughly estimate that the PKT detector with an exposure of 25 kt·yr would achieve measurement precisions of approximately 4% for the total geoneutrino flux and 27% for the Th/U ratio [41]. A 4% precision is sufficient to test hypotheses regarding the enrichment of refractory elements in the PKT inner crust. Owing to the lower geoneutrino flux, achieving the measurement precisions mentioned above would require an exposure of 216 kt·yr for the FHT detector. As shown in the lower panel of Fig. 4, the signal of the FHT detector originates mainly from the FHT crust and the FHT mantle. Therefore, a total flux measurement precision of 4% would confirm that these two reservoirs are deficient in HPEs.

B. IBD reaction on ${}^3\text{He}$

Here we utilize ${}^3\text{He}$ as the target nucleus to detect the lunar geoneutrinos through the charged current reaction:



This channel offers several significant advantages. Firstly, this reaction possesses a comparatively large cross section [42], as shown in Fig. 6. Note that the cross section used here is derived from high precision nuclear theory calculation, specifically utilizing the weak charged single-nucleon current operator and the AV18 potential for the ${}^3\text{He}$ and ${}^3\text{H}$ wave functions [42]. Secondly, the reaction product is ${}^3\text{H}$, which has a half-life of 12.32 years, allowing for accumulation over time. Most importantly, the threshold for this reaction is 1.041 MeV. Unlike the IBD threshold, this lower threshold allows for the detection of the high energy tail of ${}^{40}\text{K}$ geoneutrinos (endpoint energy 1.31 MeV). Indeed, this reaction was discussed long ago for the detection of terrestrial geoneutrinos [43]. However, it has remained experimentally impractical due to the unlikelihood of obtaining sufficient quantities of ${}^3\text{He}$ on Earth. Building on this limitation, the approach proposed here leverages the unique lunar environment, where the global inventory of ${}^3\text{He}$ amounts to about 6.5×10^5 ton in the regolith due to solar wind implantation [44], constituting a valuable resource for future fusion power and in-situ resource utilization.

We propose a radiochemical method to measure lunar geoneutrinos, mirroring the pioneering Homestake chlorine detector that used the reaction $\nu_e + {}^{37}\text{Cl} \rightarrow e^- + {}^{37}\text{Ar}$ [45]. In this scenario, ${}^3\text{H}$ generated by the reaction $\bar{\nu}_e + {}^3\text{He} \rightarrow e^+ + {}^3\text{H}$ undergoes simultaneous decay. Therefore, its net inventory over time is given by

$$N(t) = N_{\text{eq}} \times (1 - e^{-\lambda t}), \quad (3)$$

where the decay constant $\lambda = 0.0563 \text{ yr}^{-1}$ and t is the exposure time. For a given event rate R , the equilib-

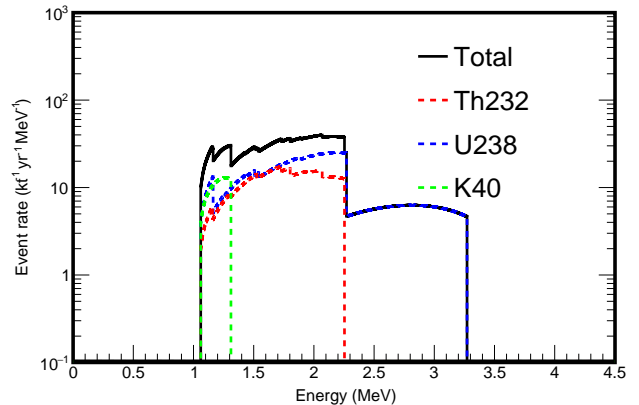


FIG. 8. Event rates of the IBD reaction on ${}^3\text{He}$ from ${}^{232}\text{Th}$, ${}^{238}\text{U}$ and ${}^{40}\text{K}$ at the PKT site.

rium number of ${}^3\text{H}$ is $N_{\text{eq}} = R/\lambda$. This substantial ratio indicates a strong accumulation effect relative to the instantaneous production rate. To estimate the accumulation number of ${}^3\text{H}$ atoms, we calculate the expected event rate for the PKT site, as shown in Fig. 8. It is clear that ${}^{40}\text{K}$ has a significant contribution. The total production rate R of ${}^3\text{H}$ is found to be $43.10 \text{ kt}^{-1} \text{ yr}^{-1}$. For illustration, we consider a 1 kt ${}^3\text{He}$ target with a 10-year exposure, yielding a net ${}^3\text{H}$ production of approximately 329.61 atoms, where the contributions from ${}^{238}\text{U}$, ${}^{232}\text{Th}$, and ${}^{40}\text{K}$ are 199.37, 110.08, and 20.16 atoms, respectively.

By separating and counting the produced ${}^3\text{H}$ from the ${}^3\text{He}$ target, we can measure the total geoneutrino rate (U+Th+K). This measured total rate, when combined with the U+Th flux obtained from the IBD reaction (Sec. IV A), allows us to derive the ${}^{40}\text{K}$ abundance. This measurement would provide a critical constraint on the Moon's volatile depletion history. Note that this radiochemical method confronts two dangerous backgrounds that produce ${}^3\text{H}$ and mimic the signal: $n + {}^3\text{He} \rightarrow p + {}^3\text{H}$ and $\mu^- + {}^3\text{He} \rightarrow \nu_\mu + {}^3\text{H}$. Both the stopped μ^- and the neutrons are largely sourced from cosmic-ray interactions with the lunar regolith: the μ^- directly, and the neutrons indirectly via the muon induced spallation reaction. To reduce these backgrounds, the detector can be buried at a sufficient depth, which serves as an effective strategy to attenuate cosmic muons and their secondary particles. The lunar environment offers an intrinsic advantage: due to the lack of a substantial atmosphere, the flux of cosmic muons is far less than that beneath the Earth's surface [34]. In addition, the ${}^3\text{He}$ target may be doped with elements such as Gd or Sm, which have higher neutron capture cross sections, and with isotopes that enhance muon capture [43], thereby competing with the two hazardous reactions. The practical implementation of this radiochemical method faces many technical challenges that require dedicated research, which extends beyond the focus of the present work.

C. Elastic scattering on electrons

The third detection channel is neutrino-electron elastic scattering, $\bar{\nu} + e^- \rightarrow \bar{\nu} + e^-$. This process has no intrinsic energy threshold, making it sensitive to the full geoneutrino spectra—a particularly important feature for detecting geoneutrinos from ^{40}K . It should be noted that $\bar{\nu}_e$, $\bar{\nu}_\mu$ and $\bar{\nu}_\tau$ all participate in elastic scattering with electrons, with their respective cross sections shown in Fig. 6 [46]. In Fig. 9, we plot the kinetic energy spectra of recoiling electrons produced by the elastic scattering reaction of geoneutrinos for the PKT detector. The expected overall elastic scattering event rate is found to be $127.16 \text{ kt}^{-1} \text{ yr}^{-1}$, with the contributions coming from ^{238}U , ^{232}Th , and ^{40}K given by 54.42, 35.91, and $36.82 \text{ kt}^{-1} \text{ yr}^{-1}$, respectively. This rate already exceeds the IBD event rate, despite the fact that the elastic scattering cross sections are much smaller. The higher rate is attributed to a far larger number of target electrons, low energy geoneutrinos below the IBD threshold ($<1.806 \text{ MeV}$), and the additional contribution from $\bar{\nu}_\mu$ and $\bar{\nu}_\tau$. However, not all elastic scattering events are suitable for the ^{40}K analysis because solar neutrinos produce a substantial background that overwhelms the signal of interest. Therefore, a detector capable of reconstructing the direction of incoming neutrinos is essential to suppress this background. Nevertheless, such directional selection would substantially reduce the number of events available for analysis.

Here we refer to the liquid scintillator Cherenkov detector scheme [47] to simply discuss the potential for detecting lunar geoneutrinos. This approach uses a slow liquid scintillator with a prolonged emission time constant (e.g., 20 ns), enabling the separation of Cherenkov and scintillation light. As a result, it allows for simultaneous energy reconstruction and directional measurement of charged particles, offering a powerful means to suppress solar neutrino backgrounds and identify geoneutrino signals. A comparison between Fig. 9 in this work and Fig. 6 in Ref. [47] reveals that the event rates from ^{238}U and ^{232}Th are about 57% of those reported in Ref. [47]. In contrast, the event rate from ^{40}K is only about 10%. This pronounced discrepancy arises from a significantly lower potassium abundance in the Moon: the K/Th ratio is around 460 [4], substantially smaller than the terrestrial value of approximately 3000 [27], indicating a greater depletion of volatile potassium in lunar materials. Based on the 10% ratio and the sensitivity curve presented in Fig. 12 of Ref. [47], and assuming similar signal efficiency and background levels, a lunar liquid-scintillator Cherenkov detector would roughly require an exposure of about $560 \text{ kt}\cdot\text{yr}$ to achieve a 3σ confidence level detection of ^{40}K geoneutrinos. Such a demanding exposure requirement appears highly impractical in the near future.

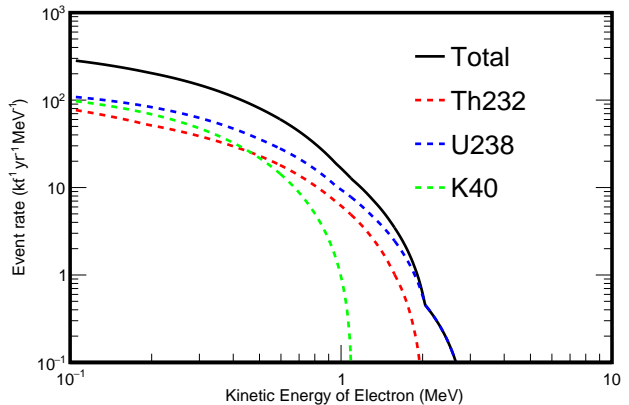


FIG. 9. Kinetic energy spectra of recoiling electrons produced by the ES reaction of geoneutrinos for the PKT detector.

V. SUMMARY

In summary, we have derived comprehensive flux estimates and evaluated detection prospects for lunar geoneutrinos. We present lunar geoneutrino flux calculations using a refined interior model for the distribution of heat-producing elements in the lunar crust and mantle, focusing on the PKT and FHT as high- and low-flux benchmarks, respectively. Notably, the flux at the PKT center is approximately 8.63 times higher than that at the FHT center, as geoneutrinos at the PKT originate almost exclusively from its inner crust, which hosts the highest abundances of heat-producing elements, whereas those at the FHT arise from comparable contributions by both its crust and mantle. We further computed the angular distributions of geoneutrinos and demonstrate that, in principle, directional detection can resolve the contributions from the FHT crust and mantle.

Finally, we evaluate the detection feasibility of lunar geoneutrinos via conventional Inverse Beta Decay (IBD), ^3He -mediated IBD, and Electron Scattering (ES) channels. At the PKT center, a nominal exposure of $25 \text{ kt}\cdot\text{yr}$ is projected to yield measurement precisions of 4% for the total flux and 27% for the Th/U ratio. Furthermore, we introduce a radiochemical method utilizing lunar ^3He as an in-situ resource to constrain U and Th abundances, offering a unique solution to the long-standing challenge of ^{40}K geoneutrino detection. In contrast, the ES channel is found to require prohibitively large exposures, rendering it impractical for near-term implementation. Ultimately, the deployment of a lunar geoneutrino observatory would provide a transformative, non-invasive probe into the Moon's deep interior, resolving longstanding questions regarding its formation, differentiation, and thermal evolution.

ACKNOWLEDGMENTS

W. L. Guo is grateful to Prof. J. Golak for sharing the precise data for the cross sections of $\bar{\nu}_e$ on ${}^3\text{He}$ in the 1.06–10 MeV range. This work is supported

in part by the National Nature Science Foundation of China (NSFC) under Grants No. 12205018, 12375098 and U2541290, and the Strategic Priority Research Program of the Chinese Academy of Sciences under Grant No. XDA10010100.

-
- [1] M. Laneuville *et al.*, Asymmetric thermal evolution of the Moon, *J. Geophys. Res. Planets* **118**, 1435–1452 (2013)
- [2] B. L. Jolliff *et al.*, Major lunar crustal terranes: Surface expressions and crust-mantle origins, *J. Geophys. Res. Planets* **105**, 4197–4216 (2000)
- [3] M. A. Wieczorek and R. J. Phillips, The “Procellarum KREEP Terrane”: Implications for mare volcanism and lunar evolution, *J. Geophys. Res. Planets* **105**, 20417–20430 (2000)
- [4] M. Laneuville, J. Taylor and M. A. Wieczorek, Distribution of radioactive heat sources and thermal history of the Moon, *J. Geophys. Res. Planets* **123**, 3144–3166 (2018)
- [5] C. K. Shearer *et al.*, Thermal and magmatic evolution of the Moon, *Rev. Mineral. Geochem.* **60**, 365–518 (2006)
- [6] M. A. Wieczorek *et al.*, The crust of the Moon as seen by GRAIL, *Science* **339**, 671–675 (2013)
- [7] M. Ohtake *et al.*, The global distribution of pure anorthosite on the Moon, *Nature* **461**, 236–240 (2009)
- [8] L. T. Elkins-Tanton, S. Burgess and Q. Z. Yin, The lunar magma ocean: Reconciling the solidification process with lunar petrology and geochronology, *Earth Planet. Sci. Lett.* **304**, 326–336 (2011)
- [9] I. Garrick-Bethell and M. T. Zuber, Elliptical structure of the South Pole-Aitken basin, *Icarus* **204**, 399–408 (2009)
- [10] D. P. Moriarty and C. M. Pieters, The character of South Pole-Aitken Basin: Patterns of surface and subsurface composition, *J. Geophys. Res. Planets* **123**, 729–747 (2018)
- [11] G. A. Snyder, L. A. Taylor and C. R. Neal, A chemical model for generating the sources of mare basalts: Combined equilibrium and fractional crystallization of the lunar magma ocean, *Geochimica et Cosmochimica Acta* **56**, 3809–3823 (1992)
- [12] H. C. Tian *et al.*, Non-KREEP origin for Chang’e-5 basalts in the Procellarum KREEP Terrane, *Nature* **600**, 59–63 (2021)
- [13] Z. Cui *et al.*, A sample of the Moon’s far side retrieved by Chang’e-6 contains 2.83-billion-year-old basalt, *Science* **386**, 1395–1399 (2024)
- [14] Q. Zhang *et al.*, Lunar farside volcanism 2.8 billion years ago from Chang’e-6 basalts, *Nature* **643**, 356–360 (2025)
- [15] G. Fiorentini, M. Lissia and F. Mantovani, Geo-neutrinos and Earth’s interior, *Phys. Rept.* **453**, 117–172 (2007)
- [16] G. Bellini *et al.*, Geoneutrinos and geoscience: an intriguing joint-venture, *La Rivista del Nuovo Cimento* **45**, 1–105 (2022)
- [17] S. Dye and A. Barna, Lunar antineutrinos and heat: fluxes from primordial radioactivity, [arXiv:2406.00882 [physics.geo-ph]]
- [18] T. Araki, S. Enomoto, K. Furuno, Y. Gando, K. Ichimura, H. Ikeda, K. Inoue, Y. Kishimoto, M. Koga and Y. Koseki, *et al.* Experimental investigation of geologically produced antineutrinos with KamLAND, *Nature* **436**, 499–503 (2005)
- [19] M. Agostini *et al.* [Borexino], Comprehensive geoneutrino analysis with Borexino, *Phys. Rev. D* **101**, no.1, 012009 (2020)
- [20] S. Abe *et al.* [KamLAND], Abundances of uranium and thorium elements in Earth estimated by geoneutrino spectroscopy, [arXiv:2205.14934 [physics.geo-ph]]
- [21] T. Adam *et al.* [JUNO], Prospects for geoneutrino detection with JUNO, [arXiv:2511.07227 [hep-ex]]
- [22] M. G. Langseth, S. J. Keihm and K. Peters, Revised lunar heat-flow values, *Proc. Lunar Planet. Sci. Conf.* **7**, 3143–3171 (1976)
- [23] S. Santangelo *et al.*, Present-day thermal state and surface heat flux of the Moon, *J. Geophys. Res. Planets* **130**, e2025JE009458 (2025)
- [24] Y. Harada *et al.*, Strong tidal heating in an ultralow-viscosity zone at the core-mantle boundary of the Moon, *Nat. Geosci.* **7**, 569–572 (2014)
- [25] R. C. Weber, P.-Y. Lin, E. J. Garnero, Q. Williams and P. Lognonné, Seismic detection of the lunar core, *Science* **331**, 309–312 (2011)
- [26] K. Lodders, Solar System Abundances and Condensation Temperatures of the Elements, *Astrophys. J.* **591**, 1220–1247 (2003)
- [27] W. F. McDonough and S. S. Sun, The composition of the Earth, *Chem. Geol.* **120**, 223–253 (1995)
- [28] S. R. Taylor and M. A. Wieczorek, Lunar bulk chemical composition: A post-Gravity Recovery and Interior Laboratory reassessment, *Philos. Trans. R. Soc. A* **372**, 20130242 (2014)
- [29] R.F. Garcia *et al.*, Very preliminary reference Moon model, *Physics of the Earth and Planetary Interiors* **188**, 96–113 (2011)
- [30] S. Enomoto, Geoneutrino spectrum and luminosity, <https://www.awa.tohoku.ac.jp/sanshiro/research/geoneutrino/spectrum/>
- [31] F. P. An *et al.* [Daya Bay Collaboration], Precision Measurement of Reactor Antineutrino Oscillation at Kilometer-Scale Baselines by Daya Bay, *Phys. Rev. Lett.* **130**, no.16, 161802 (2023)
- [32] A. Abusleme *et al.* [JUNO Collaboration], First measurement of reactor neutrino oscillations at JUNO, arXiv:2511.14593 [hep-ex] (2025)
- [33] A. K. Theinat *et al.*, Lunar lava tubes: Morphology to structural stability, *Icarus* **338**, 113442 (2020)
- [34] H. Hu, Y. P. Cheng and W. L. Guo, Lunar regolith neutrinos, in preparation
- [35] O. Šrámek *et al.*, Geophysical and geochemical constraints on geoneutrino fluxes from Earth’s mantle, *Earth Planet. Sci. Lett.* **361**, 356–366 (2013)
- [36] G. Fiorentini, M. Lissia, F. Mantovani and B. Ricci, KamLAND results and the radiogenic terrestrial heat, *Phys. Lett. B* **629**, 77–82 (2005)

- [37] M. Leyton, S. Dye and J. Monroe, Exploring the hidden interior of the Earth with directional neutrino measurements, *Nature Commun.* **8**, 15989 (2017)
- [38] H. K. M. Tanaka and H. Watanabe, 6Li-loaded directionally sensitive anti-neutrino detector for possible geoneutrino-graphic imaging applications, *Sci. Rep.* **4**, 4708 (2014)
- [39] A. Strumia and F. Vissani, Precise quasielastic neutrino/nucleon cross-section, *Phys. Lett. B* **564**, 42-54 (2003)
- [40] F. An *et al.* [JUNO], Neutrino Physics with JUNO, *J. Phys. G* **43**, no.3, 030401 (2016)
- [41] J. F. Beacom *et al.* [Jinping], Physics prospects of the Jinping neutrino experiment, *Chin. Phys. C* **41**, no.2, 023002 (2017)
- [42] J. Golak, R. Skibiński, K. Topolnicki, H. Witala, A. Grassi, H. Kamada and L. E. Marcucci, Momentum space treatment of inclusive neutrino scattering off the deuteron and trinucleons, *Phys. Rev. C* **98**, no.1, 015501 (2018)
- [43] L. M. Krauss, S. L. Glashow and D. N. Schramm, Anti-neutrinos Astronomy and Geophysics, *Nature* **310**, 191-198 (1984)
- [44] W. Z. Fa and Y. Q. Jin, Quantitative estimation of helium-3 spatial distribution in the lunar regolith layer, *Icarus* **190**, 15-23 (2007)
- [45] B. T. Cleveland, T. Daily, R. Davis, Jr., J. R. Distel, K. Lande, C. K. Lee, P. S. Wildenhain and J. Ullman, Measurement of the solar electron neutrino flux with the Homestake chlorine detector, *Astrophys. J.* **496**, 505-526 (1998)
- [46] C. Giunti and C. W. Kim, *Fundamentals of Neutrino Physics and Astrophysics*, Oxford, 2007
- [47] Z. Wang and S. Chen, Hunting potassium geoneutrinos with liquid scintillator Cherenkov neutrino detectors, *Chin. Phys. C* **44**, no.3, 033001 (2020)